



# Sea wave modeling with X-band COSMO-SkyMed<sup>©</sup> SAR-derived wind field forcing and applications in coastal vulnerability assessment

G. Benassai<sup>1</sup>, A. Montuori<sup>2</sup>, M. Migliaccio<sup>2</sup>, and F. Nunziata<sup>2</sup>

<sup>1</sup>Dipartimento di Scienze Applicate, Università di Napoli Parthenope, Napoli, Italy

<sup>2</sup>Dipartimento per le Tecnologie, Università di Napoli Parthenope, Napoli, Italy

Correspondence to: A. Montuori (antonio.montuori@uniparthenope.it)

Received: 19 September 2012 – Published in Ocean Sci. Discuss.: 17 October 2012

Revised: 14 February 2013 – Accepted: 22 February 2013 – Published: 20 March 2013

**Abstract.** In this paper, X-band COSMO-SkyMed<sup>©</sup> synthetic aperture radar (SAR) wind field data are first used to force coastal wind wave modeling for both sea wave numerical simulation and coastal vulnerability assessment purposes. The SAR-based wind field retrieval is accomplished by resolving the SAR-based wind speed and wind direction retrieval problems independently. The sea surface wind speed is retrieved through the azimuth cut-off procedure, and the sea surface wind direction is determined by the multi-resolution analysis of the discrete wavelet transform. The wind wave modeling is based on the third-generation Simulating WAVes Nearshore (SWAN) model, which is used for sea wave state estimation in coastal and inland regions. The coastal vulnerability assessment is provided by means of a key parameter, known as impact index, which evaluates the coastal risk due to the inundation of the inshore land. Experiments consist of SWAN numerical simulations run with respect to some relevant wave storms recorded in the southern Tyrrhenian Sea on 2010, with applications in coastal vulnerability assessment along the Sele coastal plain. Experimental results show the benefits of blended wind field products, provided by European Centre for Medium Weather Forecast (ECMWF) model winds and SAR-based wind field estimations, for both wind wave modeling and coastal vulnerability assessment purposes.

## 1 Introduction

The physical, chemical and biological interactions between the ocean and the atmosphere are of great applicative relevance since they affect climate variability and Earth system dynamics (Janssen, 2004; Harlan, 2005). In fact, the oceans and the atmosphere have the capability to store and exchange energy in the form of heat, moisture, and momentum, whose changes affect the climate engine of the whole planet on a large space–temporal scale (Janssen, 2004; Harlan, 2005). The monitoring and the forecasting of wind wave interaction processes become particularly critical along the coastal areas, which are highly dynamic and geomorphologically complex systems that respond in a nonlinear manner both to extreme weather conditions and, more generally, to external perturbations (Benassai, 2006; Di Paola, 2011; Alberico et al., 2012). Moreover, the impact of climate change along the coastal regions may include the presence of events that severely affect the Earth system dynamics, such as the possible increase of sea surface temperatures as well as the changes in frequency, intensity and duration of wave storms (Benassai, 2006; Di Paola, 2011; Alberico et al., 2012).

Based on this rationale, the evolution of winds, waves and the wind-driven sea circulation is of great applicative relevance not only for the modeling and the forecasting of both weather and climate, but even for the observation of oceanographic phenomena (e.g., floods, storms and tides activities) and coastal vulnerability assessment processes.

In the following, the state-of-the-art that is relevant to the wind wave modeling and the coastal vulnerability assessment is briefly described.

With respect to the wind wave modeling, advanced spectral models known as third-generation models have been developed and validated in the last decades to solve the spectral action balance equation without any a priori spectrum restrictions for the evolution of the wave growth (WAMDI Group, 1988; Tolman, 1991; Booij et al., 1999; Benassai and Ascione, 2006). These models are able to describe the physical processes of wave generation, dissipation and wave–wave interaction, overcoming the constraints of first- and second-generation wind wave models (WAMDI Group, 1988; Tolman, 1991; Booij et al., 1999; Benassai and Ascione, 2006). Moreover, third-generation models predict directional spectra and wave properties, such as significant wave height, mean wave direction and frequency, swell wave height and mean direction, and wind stress fields.

The first prototypical third-generation wave model is the WAM, where the two-dimensional wave spectrum is allowed to freely evolve without constraints on the spectral shape (WAMDI Group, 1988). Similarly, the second third-generation wind wave model, known as WAVEWATCH III (Tolman, 1997, 1999, 2009) employs a third-order numerical propagation scheme to control numerical diffusion of swell. Nowadays, the most used third-generation wind wave modeling is the Simulating WAVes Nearshore (SWAN) model, which computes random, short-crested wind-generated waves in coastal regions and inland waters (Booij et al., 1999; Benassai, 2006; Benassai and Ascione, 2006). It is based on the Eulerian formulation of the discrete spectral action density balance equation, which accounts for refractive propagation over bathymetry and current fields. Driven by boundary conditions and local wind fields, the SWAN model allows description of the processes of wind generation, white capping, quadruplet wave–wave interactions and bottom dissipation (Booij et al., 1999; Benassai, 2006; Benassai and Ascione, 2006).

All the wind wave models described above require the knowledge of sea state currents as initial information (WAMDI Group, 1988; Tolman, 1991; Booij et al., 1999; Benassai and Ascione, 2006). The analysis of sea state conditions can be created through data assimilation, where buoy or satellite altimeter measurements are combined with a background guess from a previous forecast or climatology to create the best estimate of the current conditions. It is well known that results from wind wave simulations critically depend on the quality of the driving wind fields, whose uncertainties severely impact the estimated wave properties (Teixeira et al., 1995; Holthuijsen et al., 1996). In addition to the classical forcing provided by forecasting and/or climatological winds, other sources of wind field information have been considered in the literature to force wind wave models, such as the active satellite-based microwave synthetic aperture radar (SAR) (Johannessen et al., 2000; Portabella,

2002; Monaldo et al., 2005). The latter is considered a key alternative source of wind field information able to integrate classical wind field estimation techniques (e.g., meteorological models, in situ observations and scatterometers) due to its high spatial and temporal resolution as well as its ground coverage and short revisit time (Migliaccio and Repucci, 2006; Yang et al., 2011). Within such a framework, the possibility to retrieve the sea surface wind field from SAR data and then exploit the suitability of this information to force coastal wind wave modeling is very interesting from both scientific and operational viewpoints.

With respect to the coastal vulnerability assessment (CVA), different procedures are proposed in the literature that can be distinguished in semi-quantitative and quantitative approaches (Benassai, 2006). The first ones are mainly based on the subjective assessment of geomorphologic indicators, while the second ones quantify the relative importance of physical and geomorphologic relevant phenomenon. The proposed methodologies have been progressively evolved from single approaches, such as Bruun rule (Bruun, 1962) and UNEP methodology (Carter et al., 1994), to more recent consistent techniques, such as USGS-CVI (Gornitz et al., 1994) and SURVAS (Nicholls and de la Vega-Leinert, 2000; Benassai et al., 2009). The latter provide improved consideration of both physical and nonphysical factors, with the associated uncertainties.

One of the most used CVA methods is based on the Coastal Vulnerability Index (CVI) (Gornitz et al., 1994, 1997), which combines the changing susceptibility of the coastal system with its inherent capability to a changing environment. The vulnerability classification is based upon the relative contributions and interactions of six variables, i.e., mean elevation, geology, coastal landform, shoreline, wave height and tidal range (Diez et al., 2007).

A different approach has been recently suggested (Benassai et al., 2009), which evaluates the coastal risk due to the inundation of the inshore land. This method allows assessment of the coastal vulnerability by means of a new parameter known as impact index, which is based on wave, climate, bathymetry and sediment data. It depends on run-up height, seasonal and long-term erosion index, and efficiency of coastal protection structures (Benassai et al., 2009).

In this paper both sea wave simulations and the CVA are investigated in a coastal environment by first using X-band COSMO-SkyMed<sup>®</sup> (hereinafter CSK<sup>®</sup>) SAR-based wind field retrievals as input wind field forcing. The SAR-based wind speed and wind direction retrievals are independently accomplished using the azimuth cut-off procedure and the multi-resolution analysis of the discrete wavelet transform (MRA-DWT), respectively. SWAN numerical simulations are carried out with respect to some relevant wave storms by using different wind field forcings, i.e., European Centre for Medium Weather Forecast (ECMWF) model winds, SAR-based wind field (i.e., wind speed and direction)

retrievals and ECMWF-SAR blended wind fields. The output of SWAN simulations is then used for CVA purposes to evaluate the impact index of a coastal environment. The suitability of ECMWF-SAR blended wind field product is finally investigated for wind wave modeling and CVA purposes.

The paper is organized as follows: the test area and the data set used in this study are given in Sect. 2. The theoretical background and the methodology at the basis of the X-band SAR wind field retrieval, the wind wave model and the CVA are given in Sect. 3. Experimental results are presented and discussed in Sect. 4. Finally, conclusions are drawn in Sect. 5.

## 2 Data set

In this section, the test area and the data set used for SAR-based wind field retrieval, wind wave numerical simulations and CVA purposes are described.

The test area is the coastal zone of the southern Tyrrhenian Sea, including the Gulfs of Gaeta, Napoli, Salerno and Policastro, which are of great applicative relevance for both oceanographic and coastal-maritime surveillance purposes.

The data set consists of the following:

- 60 X-band VV-polarized Level 1B Multi-Look Ground Detected (DGM) ScanSAR Huge Region CSK<sup>®</sup> SAR data, gathered in the test area during the winter season of 2010 (Italian Space Agency, 2007). They provide ground coverage of about 200 km × 200 km with a spatial resolution of 100 m × 100 m. Each SAR scene is characterized by large variability for the incidence angle  $\theta$  ( $\sim 10^\circ$ ) and the whole SAR data set covers a broad range of  $\theta$  values (25–60°). Each Level 1B DGM SAR scene is characterized by  $\sim 18$  looks (Italian Space Agency, 2007). The SAR data set is used to retrieve the sea surface wind field (i.e., wind speed and wind direction) information according to the X-band SAR-based wind field estimation methodology described in Sect. 3.
- Timely and spatially co-located Advanced Scatterometer (ASCAT) wind fields (freely available at <http://podaac.jpl.nasa.gov/>) with a spatial gridding resolution of 12.5 km × 12.5 km in range and azimuth directions, respectively. The ASCAT scatterometer wind field is used as reference ground truth to evaluate both the effectiveness and the corresponding uncertainties of X-band CSK<sup>®</sup> SAR-based wind field estimations.
- Timely and spatially co-located ECMWF model wind data (available at: <http://www.ecmwf.int/>), with a spatial gridding resolution of  $1/4^\circ$  ( $\sim 28$  km × 20 km in range and azimuth directions, respectively) and a time resolution of 6 h. The ECMWF model winds are used together with X-band CSK<sup>®</sup> SAR-based wind field estimations to construct a blended wind field product as forcing of

both the wind wave modeling and the CVA approach described in Sect. 3.

- Timely and spatially co-located wave field data provided by in situ national buoy system observations (available on line at: [http://www.idromare.it/analisi\\_dati.php](http://www.idromare.it/analisi_dati.php)) off the isle of Ponza. The buoy-related wind wave information is used as reference ground truth for both wind wave modeling and CVA purposes.

## 3 Methodology

In this section the theoretical background and the methodology at the basis of the X-band SAR-based wind field retrieval, the wind wave simulations and the CVA are given.

### 3.1 X-band SAR wind field retrieval algorithm

The methodology and the physical background of the X-band SAR-based wind field retrieval approach is now presented and specialized for X-band VV-polarized Level 1B DGM ScanSAR Huge Region mode CSK<sup>®</sup> SAR data.

The proposed approach consists of two subsequent steps, and each of these is made of two sub-steps. At the first step, the SAR image quality is improved, while at the second step the sea surface wind field is retrieved through X-band SAR measurements.

SAR-based wind field estimation is strongly affected by SAR data quality; hence, a pre-processing analysis is necessary to improve SAR image quality. In fact, on the one hand, X-band SAR data may be affected by tropospheric and atmospheric phenomena (e.g., rain cells, cloud coverage, oceanic fronts, convective cells, etc.) that, especially at higher frequencies, can drastically hamper the SAR imagery interpretability and therefore also the retrieval of some meaningful geophysical parameters, such the sea surface wind field (Lee et al., 1995). On the other hand, the peculiar burst acquisition mode of ScanSAR SAR measurements is characterized by the presence of the scalloping, i.e., periodic processing anomalies appearing as bars in SAR imagery, which strongly affects the accuracy of SAR-based wind field estimation (Schiavulli et al., 2011, 2012).

Hence, an automatic two-sub-steps pre-processing procedure, first developed in Schiavulli et al. (2011), is used to improve the quality of SAR images. The first sub-step aims at removing the scalloping pattern by means of a MRA-DWT filtering technique (Mallat, 1989; Schiavulli et al., 2011, 2012). This approach naturally describes the directional features of an image at different spatial scales, and therefore it is able to first highlight and then remove the scalloping pattern in ScanSAR SAR measurements. As demonstrated in Schiavulli et al. (2011, 2012) for this CSK<sup>®</sup> SAR data product, the end user has no access to the SAR raw data and then only a suboptimal de-scalloping post-processing procedure can be implemented. It is worth noting that Italian

Space Agency, after the illustration of these results, claimed for a new SAR raw data processing chain to be developed in the future. The second sub-step of the pre-processing procedure filters out all the atmospheric phenomena by means of a phenomenological homogeneity test based on the variance-to-mean-square ratio (VMSR) of SAR image power spectral density (Schultz-Stellenfleth et al., 2004; Schiavulli et al., 2011). This sub-step univocally discriminates between homogeneous, i.e., sea, and non-homogeneous parts of SAR images, such as ships, coastline and atmospheric fronts.

The second step of the X-band SAR-based wind field retrieval consists in providing independent estimates of sea surface wind speed (sub-step one of step two) and wind direction (sub-step two of step two).

The SAR-based wind speed estimation is accomplished by means of an algorithm based on the azimuth cut-off procedure (Chapron et al., 1995; Kerbaol, 1998; Korsbakken et al., 1998; Migliaccio et al., 2012; Montuori et al., 2012), which allows retrieval of the sea surface wind speed without requiring both any a priori wind direction information and the calibration accuracy of SAR normalized radar cross section (NRCS) measurements of the observed scene. The physical rationale at the basis of the azimuth cut-off procedure lies on the well-known azimuthal Doppler misregistration due to the orbital motion of sea surface waves (Chapron et al., 1995; Kerbaol, 1998; Korsbakken et al., 1998). The latter affects the sea surface SAR imaging and depends on both sensor's parameters (e.g., platform altitude, velocity, etc.) and sea surface geophysical parameters (Chapron et al., 1995; Kerbaol, 1998; Korsbakken et al., 1998). Moreover, it limits the shortest detectable wavelength in the azimuth direction  $\lambda_c$ , which is a key cinematic parameter that, accounting for sea waves orbital motions within SAR integration time, can be considered a robust indicator of the sea surface wind speed (Chapron et al., 1995; Kerbaol, 1998; Korsbakken et al., 1998). Based on this rationale, a SAR wind speed algorithm based on the azimuth cut-off procedure has been developed and tested for C-band SAR measurements only (Chapron et al., 1995; Kerbaol, 1998; Korsbakken et al., 1998). Following this approach,  $\lambda_c$  is retrieved from the noise-free SAR autocorrelation function (ACF) and physically related to the sea surface wind speed using a linear semi-empirical model:

$$U_{10} = a(\lambda_c - \Lambda), \quad (1)$$

where  $U_{10}$  ( $\text{m s}^{-1}$ ) is the wind speed at 10 m above the sea surface,  $\Lambda$  (m) is the SAR nominal azimuth resolution and  $a$  ( $1 \text{ s}^{-1}$ ) is an empirical parameter. The physical rationale of the azimuth cut-off procedure has been recently extended and tested using X-band VV-polarized Level 1B DGM ScanSAR Huge Region CSK<sup>®</sup> SAR measurements (Migliaccio et al., 2012; Montuori et al., 2012).

The SAR-based wind direction estimation is accomplished by using the MRA-DWT approach (Du et al., 2002; Horstmann et al., 2002; Schiavulli et al., 2011). The rationale

of this technique relies on the fact that some wind-induced pattern texture features on the sea surface are aligned to the local wind field. These features, which are visible on SAR imagery, are interpreted as manifestations of either atmospheric boundary layer (ABL) rolls, which account for interactions between the atmosphere and the sea surface, or other marine features, such as streaks from foam or, more generally, marine surfactants (Du et al., 2002; Horstmann et al., 2002; Schiavulli et al., 2011). These phenomena appear in SAR imagery as adjacent periodic bands of bright and dark radar returns, thus resulting as image streaks that are supposed to be aligned with the mean local sea surface wind field (Du et al., 2002; Horstmann et al., 2002; Schiavulli et al., 2011). Based on this rationale, the proposed approach aims at providing the wind direction estimation at sea by simply retrieving the orientations of these wind-induced phenomena. In fact, the MRA-DWT approach allows obtainment of wind direction information by analyzing the SAR imagery at different scales, in both time and frequency domain (Mallat, 1989; Du et al., 2002; Schiavulli et al., 2011). The estimated wind direction presents an inherent  $180^\circ$  wind direction ambiguity, which can be properly solved either if wind shadowing is present in SAR imagery or by using external information, such as the ASCAT scatterometer data. The processing chain relevant to the SAR wind direction retrieval technique is detailed in Du et al. (2002) and Schiavulli et al. (2011).

### 3.2 The SWAN model

The wind wave modeling used in this work is based on the SWAN model, a third-generation numerical wave model that allows computation of random, short-crested waves in coastal regions with shallow water and ambient currents (Holthuisen et al., 1993; Booij et al., 1999; Benassai, 2006; Benassai and Ascione, 2006). It describes the temporal and spatial variation of the wind induced surface elevation, the white-capping effects and the friction with the sea bottom layer (Holthuisen et al., 1993; Booij et al., 1999; Benassai, 2006; Benassai and Ascione, 2006). In the SWAN model, the waves are described with the two-dimensional wave action density spectrum  $N = F/\sigma$  ( $F$  is the spectrum and  $\sigma$  is the intrinsic frequency) even when nonlinear phenomena dominate (e.g., in the surf zone). The action density spectrum  $N$  is considered rather than the energy density spectrum  $E(\sigma, \theta)$ , since in the presence of ambient currents only the action density is conserved (Whitham, 1974). The evolution of the wave spectrum is described by the spectral action balance equation (Hasselmann et al., 1973)

$$\frac{\partial}{\partial t} N + \frac{\partial}{\partial x} c_x N + \frac{\partial}{\partial y} c_y N + \frac{\partial}{\partial \sigma} c_\sigma N + \frac{\partial}{\partial \theta} c_\theta N = \frac{S}{\sigma}, \quad (2)$$

where  $S$  is the source function representing the sum of wave energy input from wind, energy dissipation by wave breaking and the energy redistribution via nonlinear interaction

among frequency components. The first term on the left-hand side of Eq. (2) represents the timely change rate of the local action density spectrum. The second and third term on the left-hand side of Eq. (2) represents the propagation of the action density spectrum in the Cartesian coordinates space, with propagation velocities  $c_x$  and  $c_y$ . The fourth term on the left-hand side of Eq. (2) represents the shifting of the relative frequency in the action density spectrum due to variations in depths and currents, with a propagation velocity  $c_\sigma$ . The fifth term on the left-hand side of Eq. (2) represents both the depth- and the current-induced refraction of the local action density spectrum, with propagation velocity  $c_\theta$ . The term at the right-hand side of Eq. (2) is the source term of the energy density, representing the effects of generation, dissipation, and nonlinear wave–wave interactions.

The SWAN model has been operational at Dipartimento di Scienze Applicate (DSA) of the Università degli Studi di Napoli Parthenope since January 2005 and has been adopted for simulating both waves generation and propagation in the Gulf of Naples. The model is typically forced using the wind field at 1-h intervals provided by the Advanced Research Weather Research and Forecast (WRF-ARW) wind field model data, i.e., the next-generation mesoscale numerical weather model predictions that are designed to serve both operational forecasting and atmospheric research needs (Holthuisen et al., 1993; Booij et al., 1999; Benassai, 2006; Benassai and Ascione, 2006). The model is implemented on nested grids, with a numerical propagation scheme, which makes the numerical code quite effective in shallow water (Holthuisen et al., 1993; Booij et al., 1999; Benassai, 2006; Benassai and Ascione, 2006). Outputs of the SWAN model include significant wave height ( $H_S$ ) on gridded fields, with the associated wave directions ( $D_W$ ) and periods ( $T_P$ ), and the wave energy spectral information at different wavelengths.

### 3.3 The CVA model

The CVA approach used in this paper is based on the methodology first proposed in Benassai et al. (2009), where a new key parameter, known as impact index  $I_i$  is defined for the coastal flooding risk evaluation. This parameter accounts for wave climate, bathymetry and sediment data and depends on the wave run-up height, the seasonal and long-term erosion index, and the efficiency of coastal protection structures. It is given by Benassai et al. (2009):

$$I_i = I_{Ru} + I_R + I_D + E + T, \quad (3)$$

where  $I_{Ru}$  is an inundation distance index associated to the wave run-up,  $I_R$  is the short-term erosion index for the shoreline,  $I_D$  is the index of stability for backshore coastal protection structures,  $E$  is the long-term erosion index and  $T$  is the tidal range. Compared to the main CVA methods, this methodology can be applied on a small geographical scale for coastal flooding risk evaluation. Moreover, it must be

noted that in Benassai et al. (2009) the tidal effects are not considered since applied to a micro-tidal environment, i.e. the Mediterranean Sea.

Here the CVA is carried out by evaluating Eq. (3) without considering  $I_D$  and  $T$  index contributions. In fact, the test area (i.e., the southern Tyrrhenian Coastal Sea basin) is a micro-tidal coastal environment (hence,  $T = 0$ ) where no coastal protection is present (hence,  $I_{D=0}$ ). Therefore, only  $I_{Ru}$ ,  $I_R$  and  $E$  contributions will be taken into account for the evaluation of  $I_i$ .

The  $I_{Ru}$  index provides the measurement of the potential inundation capacity, which characterizes natural beaches with respect to wave storms.  $I_{Ru}$  assumes values that depend on the percentage associated to the maximum horizontal wave run-up distance on the beach ( $X_{max}$ ) normalized with respect to the emerged beach width ( $L$ ) (Benassai et al., 2009).  $X_{max}$  is retrieved through the wave run-up height, which depends on both beach and wave properties:

$$X_{max} = \frac{R_{2\%}}{\tan(\beta)}, \quad (4)$$

where  $\beta$  is the tidal beach slope and  $R_{2\%}$  is the 2% exceedance level for wave run-up peaks. The latter is retrieved through the empirical approach proposed in Stockdon et al. (2006):

$$R_{2\%} = 1.1 \cdot \left( 0.35 \cdot \beta_f \cdot \sqrt{H_0 \cdot L_0} + \frac{\sqrt{H_0 \cdot L_0 \cdot (0.563\beta_f^2 + 0.004)}}{2} \right), \quad (5)$$

where  $\beta_f$  is the foreshore beach slope defined over the area of significant swash activity (it is approximated to  $\beta$ ),  $H_0$  is the foreshore wave height (it can be approximated to  $H_S$ ) and  $L_0$  is the foreshore wave length evaluated as function of  $T_P$  (Benassai et al., 2009).

Based on Eqs. (4) and (5) and according both to  $X_{max}$  and  $L$  estimates,  $I_{Ru}$  values can be customarily clustered into four discrete levels (Benassai et al., 2009):

$$I_{Ru} = \begin{cases} 1 & \text{if } \frac{X_{max}}{L} \% < 40 \\ 2 & \text{if } 40 \leq \frac{X_{max}}{L} \% < 60 \\ 3 & \text{if } 60 \leq \frac{X_{max}}{L} \% < 80 \\ 4 & \text{if } \frac{X_{max}}{L} \% \geq 80 \end{cases}, \quad (6)$$

where  $I_{Ru}$  values are mapped into four categories of the short-term vulnerability according to the classification rule defined in Benassai et al. (2009), i.e., stable ( $I_{Ru} = 1$ ), low ( $I_{Ru} = 2$ ), moderate ( $I_{Ru} = 3$ ) and high ( $I_{Ru} = 4$ ) short-term erosion of the natural beach (see Table 1).

The  $I_R$  index provides a measurement of potential beach retreat and is used for the dynamical calculation of the shoreline retreat based on the convolution method of Kriebel and Dean (1993).  $I_R$  values depend on the percentage associated to the maximum beach retreat ( $R_{max}$ ) normalized with respect to  $L$  (Benassai et al., 2009).  $R_{max}$  is evaluated as

**Table 1.** Classification of  $I_R$ ,  $I_{Ru}$ ,  $E$  and  $I_i$  index values.

Class	Stability	Low	Moderate	High
Value	1	2	3	4
$I_R$	$R_{\max}/L \% < 15$	$15 \leq R_{\max}/L \% < 30$	$30 \leq R_{\max}/L \% < 50$	$R_{\max}/L \% \geq 50$
$I_{Ru}$	$X_{\max}/L \% < 40$	$40 \leq X_{\max}/L \% < 60$	$60 \leq X_{\max}/L \% < 80$	$X_{\max}/L \% \geq 80$
$E$	$V_E (\text{m yr}^{-1}) < 0.5$	$0.5 \leq V_E (\text{m yr}^{-1}) < 1.0$	$1.0 \leq V_E (\text{m yr}^{-1}) < 2.0$	$V_E (\text{m yr}^{-1}) \geq 2.0$
$I_i$	3.0	4.0–6.0	7.0–9.0	10.0–12.0

the maximum value of the general solution associated to the Kriebel and Dean (1993) convolution method

$$\frac{R(t)}{R_\infty} = \frac{1}{2} \left\{ 1 - \frac{\gamma^2}{1 + \gamma^2} \exp(-2\sigma t / \gamma) - \frac{1}{1 + \gamma^2} [\cos(2\sigma t) + \gamma \sin(2\sigma t)] \right\}, \quad (7)$$

where

$$R_\infty = S \frac{W_b - d_b / m_0}{B + d_b - S/2}. \quad (8)$$

$S$  is the sea level increase due to the wave storm (it is directly proportional to  $H_s$ ),  $B$  is the berm height,  $m_0$  is the foreshore seabed slope,  $d_b$  is the breaking depth (it is directly proportional to  $H_s$ ),  $W_b$  is the offshore breaking depth distance (it is inversely proportional to the median dimension of beach sediments  $\mu_s$ ),  $\sigma$  is the angular frequency associated to  $T_p$ ,  $\gamma$  is the ratio between the beach system time scale  $T_s$  and the wave storm duration  $T_D$  (Benassai et al., 2009).

Based on Eqs. (7) and (8) and according to both  $R_{\max}$  and  $L$  estimates,  $I_R$  values can be customarily clustered into four discrete levels (Benassai et al., 2009):

$$I_R = \begin{cases} 1 & \text{if } \frac{R_{\max}}{L} \% < 40 \\ 2 & \text{if } 40 \leq \frac{R_{\max}}{L} \% < 60 \\ 3 & \text{if } 60 \leq \frac{R_{\max}}{L} \% < 80 \\ 4 & \text{if } \frac{R_{\max}}{L} \% \geq 80 \end{cases}, \quad (9)$$

where  $I_R$  values are properly mapped into four categories of the short-term vulnerability according to the classification rule defined in Benassai et al. (2009), i.e., stable ( $I_R = 1$ ), low ( $I_R = 2$ ), moderate ( $I_R = 3$ ) and high ( $I_R = 4$ ) short-term erosion of natural beach (see Table 1).

The  $E$  index provides the long-term evaluation of potential beach retreat and is measured by comparing photogrammetric flights of different years relevant to the observed test area. It assumes values that depend on the beach erosion rate  $V_E$  ( $\text{m yr}^{-1}$ ) (Benassai et al., 2009):

$$E = \begin{cases} 1 & \text{if } V_E (\text{m yr}^{-1}) < 0.5; \\ 2 & \text{if } 0.5 \leq V_E (\text{m yr}^{-1}) < 1 \\ 3 & \text{if } 1 \leq V_E (\text{m yr}^{-1}) < 2 \\ 4 & \text{if } V_E (\text{m yr}^{-1}) \geq 2 \end{cases}, \quad (10)$$

where  $E$  values are properly mapped into four categories of the long-term vulnerability according to the classification rule defined in Benassai et al. (2009), i.e., stable ( $E = 1$ ), low ( $E = 2$ ), moderate ( $E = 3$ ) and high ( $E = 4$ ) long-term erosion of the natural beach (see Table 1).

Based on the definition of both short- and long-term erosion indexes, the impact index  $I_i$  is evaluated according to Eq. (3). Based on the customary classification of  $I_{Ru}$ ,  $I_R$  and  $E$  parameters,  $I_i$  values are mapped into four categories of coastal vulnerability risk according to the classification rule defined in Benassai et al. (2009), i.e., stable ( $I_i = 3$ ), low ( $3 < I_i \leq 6$ ), moderate ( $6 < I_i \leq 9$ ) and high ( $9 < I_i \leq 12$ ) vulnerability risk of natural beach (see Table 1).

## 4 Experimental results

In this section some meaningful experimental results are presented and discussed to show the benefits of X-band CSK<sup>©</sup> SAR-based wind field estimations for the improvement of both wind wave modeling and coastal vulnerability assessment. They are relevant to the application of the SWAN model in a coastal environment and the subsequent assessment of the coastal vulnerability, with forcing provided by X-band CSK<sup>©</sup> SAR-derived wind field estimations.

### 4.1 SAR wind field retrieval

First of all, a preliminary analysis on the effectiveness of the X-band SAR wind field retrieval is undertaken by using X-band CSK<sup>©</sup> SAR data described in Sect. 2.

The wind field retrieval is undertaken using a gridding scale of  $12.5 \text{ km} \times 12.5 \text{ km}$  along with the range and azimuth directions, respectively. The reference ground truth used for comparison and validation purposes is provided by timely and spatially co-located  $12.5 \text{ km} \times 12.5 \text{ km}$  ASCAT scatterometer wind fields. In the particular case where the ASCAT scatterometer wind field is not available for the SAR acquisition, the reference ground truth is then provided by  $28 \text{ km} \times 20 \text{ km}$  ECMWF model data. To properly co-locate the reference ground truth and the SAR-based wind field estimation, both a linear interpolation in time and a bilinear spatial interpolation onto the SAR-based wind field retrieval gridding scale is accomplished.

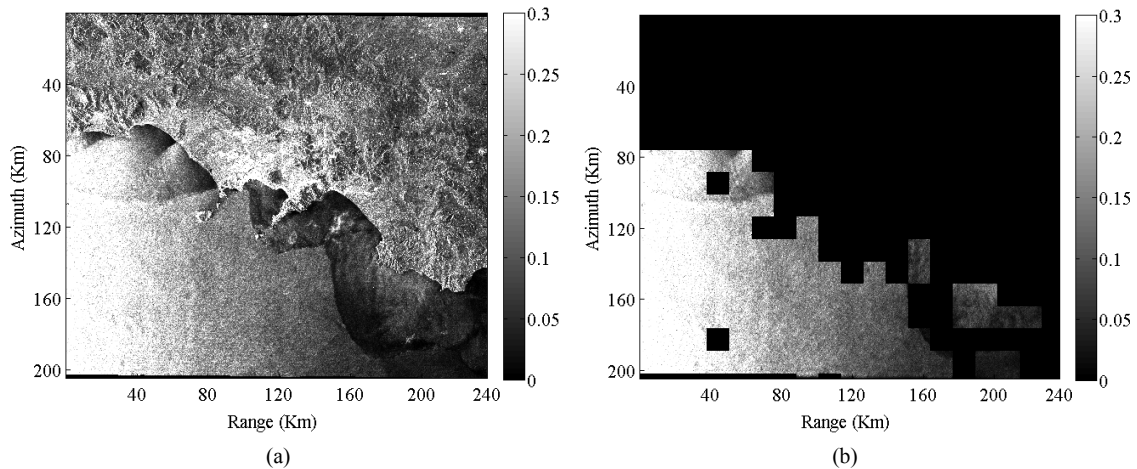


**Fig. 1.** X-band Level 1B DGM ScanSAR Huge Region CSK<sup>®</sup> SAR data acquired on 17 December 2010 at 18:00 UTC. (a) VV-polarized NRCS. (b) Output of the pre-processing step relevant to the SAR wind field retrieval approach.

A single experiment is fully detailed to demonstrate the consistency of the X-band CSK<sup>®</sup> SAR-derived wind field retrieval, taking full benefits of VV-polarized Level 1B DGM ScanSAR Huge Region mode CSK<sup>®</sup> SAR data.

The experiment is relevant to the X-band CSK<sup>®</sup> SAR acquisition of 17 December 2010 at 18:00 UTC, which refers to an interesting winter wave storm that occurred in the coastal area of the Tyrrhenian Sea on 2010. The VV-polarized NRCS image is shown in gray tones in Fig. 1a, where the scalloping effect and weak atmospheric phenomena are present. The output of the pre-processing step is shown in Fig. 1b, where the land is masked out. It must be noted that SAR image quality is improved both by reducing the scalloping effect and by filtering out atmospheric phenomena.

The output of the wind speed retrieval is shown in Fig. 2a together with the reference timely and spatially co-located ECMWF and ASCAT ground truth (see Fig. 2b–c, respectively). It must be noted that in this particular case, the ASCAT scatterometer ground truth does not cover the whole spatial domain of the SAR acquisition (see Fig. 2c–d). The comparison between the SAR-based wind speed estimation and the reference ground truth (both the scatterometer- and the model-based wind speed) shows a fair agreement with root mean square error (RMSE) values lower than  $3 \text{ m s}^{-1}$ . In fact, the CSK<sup>®</sup> SAR-ASCAT and CSK<sup>®</sup> SAR-ECMWF wind speed inter-comparisons provide RMSE values equal to  $0.96 \text{ m s}^{-1}$  and  $1.9 \text{ m s}^{-1}$ , respectively. Experimental results demonstrate that the X-band CSK<sup>®</sup> SAR wind speed estimations provided at the gridding scale of  $12.5 \text{ km} \times 12.5 \text{ km}$  are consistent and effectively comparable with the reference ground truth. This result further demonstrates the physical soundness of the SAR-based wind speed retrieval approach showing the effectiveness of the X-band azimuth cut-off model function. However, it can be noted that non-negligible

differences in terms of sea surface wind speed are present closer to the coastal area of the SAR image domain for both the ECMWF and ASCAT scatterometer winds. This could be explained by taking into account that the reference ASCAT scatterometer and ECMWF model wind speeds are available at the resolution gridding scale of  $12.5 \text{ km} \times 12.5 \text{ km}$  and  $28 \text{ km} \times 20 \text{ km}$ , respectively.

The output of the SAR-based wind direction retrieval is shown in Fig. 3a–b, together with the timely and spatially co-located ECMWF and ASCAT scatterometer-based wind direction, respectively. The comparison between the SAR-based wind direction estimation and the reference ground truth (both the scatterometer- and the model-based wind direction) shows a fair agreement with RMSE values equal to  $6^\circ$  and  $12^\circ$  for the CSK<sup>®</sup> SAR-ASCAT and the CSK<sup>®</sup> SAR-ECMWF wind direction inter-comparisons, respectively. Experimental results agree with previous ones, demonstrating that some of the differences observed between the reference ground truth and the X-band SAR-based MRA-DWT wind direction retrievals can be explained by considering the different spatial gridding resolution scale of both modeled (ECMWF) and remotely sensed (SAR and ASCAT) wind direction estimation products.

Other results are summarized in the scatter plots of Fig. 4, where the  $12.5 \text{ km} \times 12.5 \text{ km}$  SAR-based wind speed and wind direction retrievals are compared with respect to the ASCAT scatterometer reference wind speed and wind direction, respectively, for the whole CSK<sup>®</sup> SAR data set. The comparison between the X-band SAR-based wind field retrievals and ECMWF model winds will be presented in the next section in terms of sea wave numerical simulations. Experimental results agree with the previous ones, thus demonstrating the consistency of SAR-derived wind field estimations with respect to the ASCAT scatterometer reference ground truth. In detail, the CSK<sup>®</sup> SAR-ASCAT wind

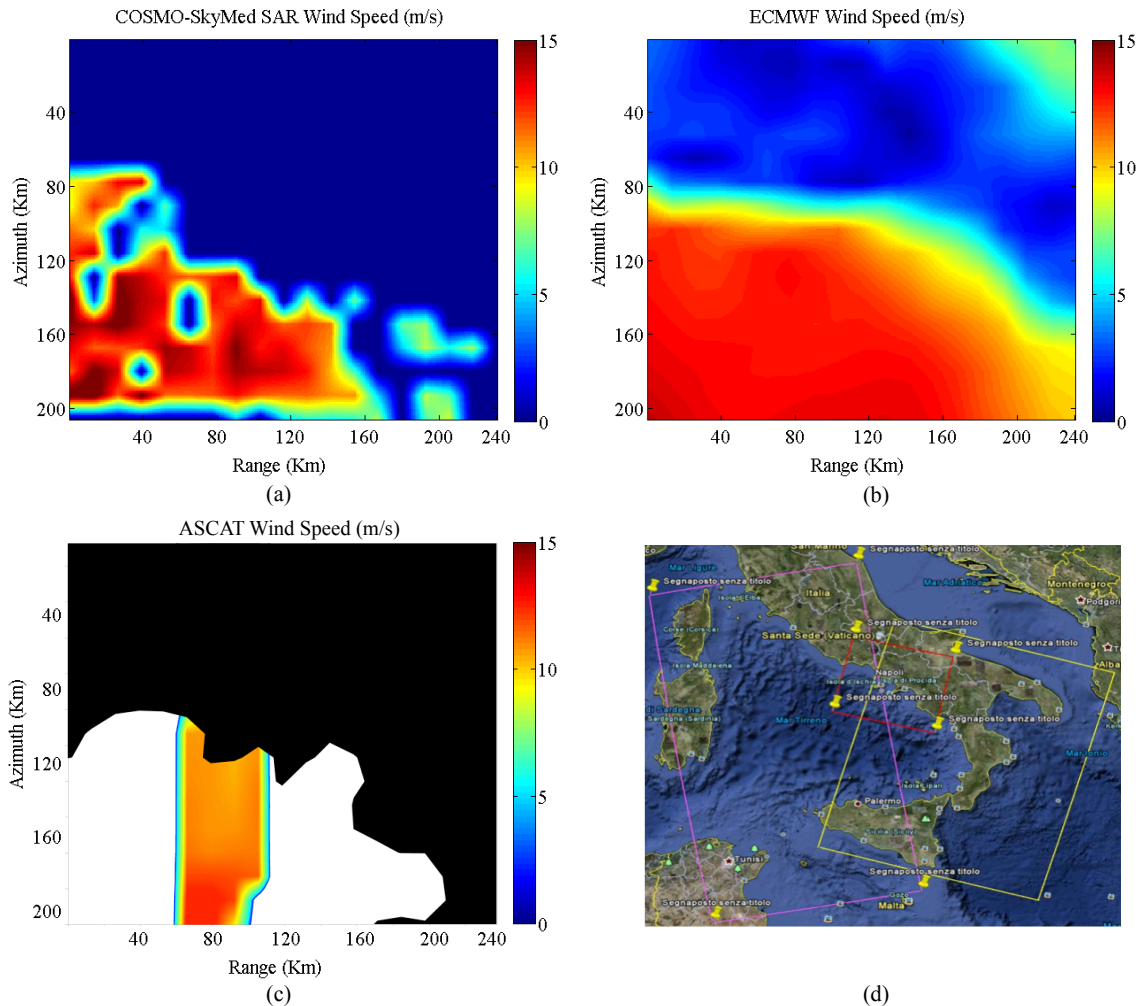


**Fig. 2.** Experimental results relevant to the SAR-based wind speed estimation for the X-band Level 1B DGM ScanSAR Huge Region CSK<sup>®</sup> SAR data acquired on 17 December 2010 at 18:00 UTC. **(a)** X-band SAR-derived wind speed estimation over a sub-image scale of 12.5 km × 12.5 km. **(b)** Timely and spatially co-located ECMWF model wind speed. **(c)** Timely and spatially co-located ASCAT scatterometer wind speed. **(d)** Footprints of the ASCAT scatterometer wind speeds acquired before (purple box) and after (yellow box) the SAR acquisition, whose footprint is shown red color.

speed inter-comparison (see Fig. 4a) provides a mean error ( $\mu$ ) value of  $-0.73 \text{ m s}^{-1}$ , a standard deviation ( $\sigma$ ) value of  $2.07 \text{ m s}^{-1}$  and an RMSE value of  $2.19 \text{ m s}^{-1}$ . On the other hand, the CSK<sup>®</sup> SAR-ASCAT wind direction inter-comparison (see Fig. 4b) provides a  $\mu$  value of  $1.71^\circ$ , a  $\sigma$  value of  $18.88^\circ$  and an RMSE value of  $18.95^\circ$ . These results demonstrate the consistency of X-band SAR-derived wind field retrievals with respect to the ASCAT scatterometer ground truth. This latter suffers from uncertainty over the maritime coastal areas and it is not able to capture small-scale features, which can in turn be revealed by means of SAR data. Such results demonstrate the effectiveness of both the X-band azimuth cut-off model function and the MRA-DWT technique presented in Sect. 2.1 to get consistent wind speed and wind direction estimation, respectively, even using

X-band SAR data. Furthermore, experimental results show the full benefits of X-band Level 1B DGM ScanSAR Huge Region mode CSK<sup>®</sup> SAR data as an alternative source of wind field estimation.

In summary, the wind speed is retrieved with a RMSE value of about  $2 \text{ m s}^{-1}$ , and this result is in agreement with that experienced in the C-band azimuth cut-off literature (Chapron et al., 1995; Kerbaol, 1998; Korsbakken et al., 1998). The wind direction is retrieved with a RMSE value lower than  $20^\circ$ , and this result is in total accordance with the relevant literature (Du et al., 2002; Horstmann et al., 2002; Schiavulli et al., 2011).

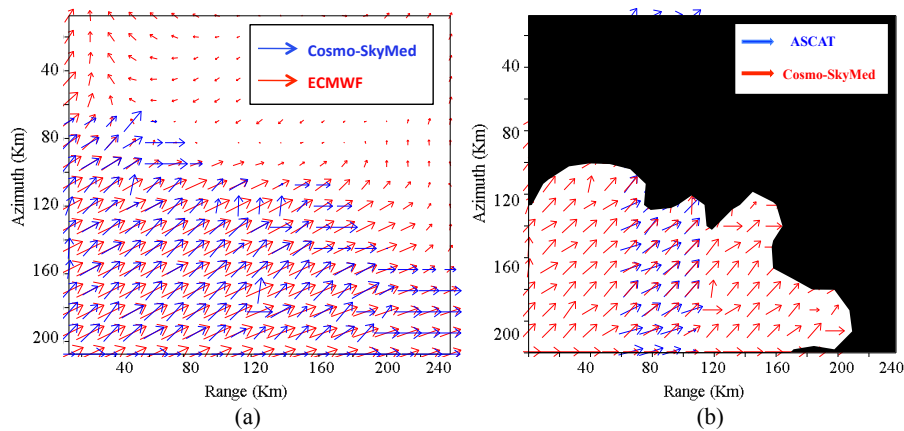


**Fig. 3.** Experimental results relevant to the SAR-based wind direction estimation for the X-band Level 1B DGM ScanSAR Huge Region CSK<sup>®</sup> SAR data acquired on 17 December 2010 at 18:00 UTC. **(a)** Comparison between X-band SAR-derived wind direction estimation and the reference ECMWF model wind direction over a sub-image scale of  $12.5 \text{ km} \times 12.5 \text{ km}$ . **(b)** Comparison between X-band SAR-derived wind direction estimation and the reference ASCAT scatterometer wind direction over a sub-image scale of  $12.5 \text{ km} \times 12.5 \text{ km}$ .

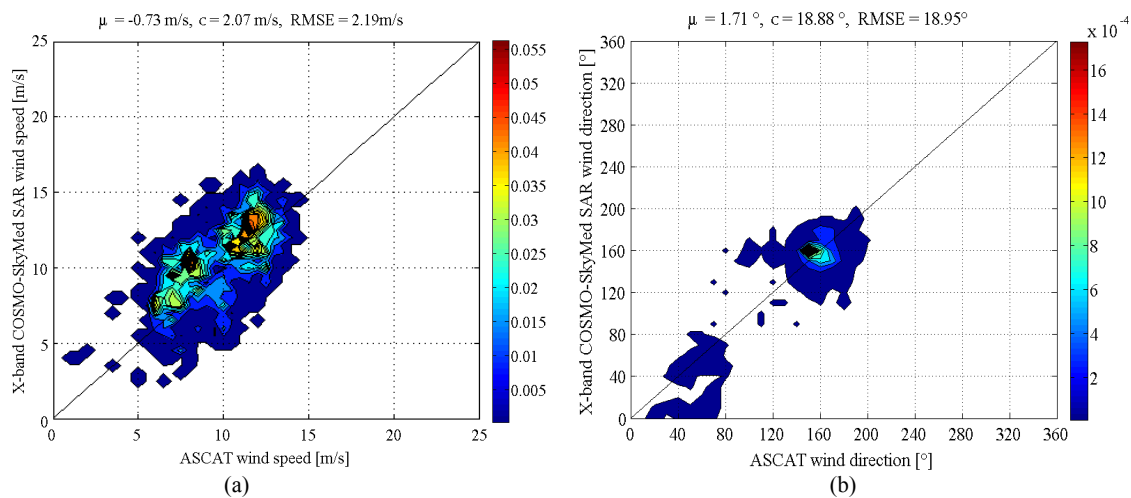


**Fig. 4.** 2-D probability density scatter plot relevant to the comparison between the  $12.5 \text{ km} \times 12.5 \text{ km}$  X-band CSK<sup>®</sup> SAR-derived wind field estimation and the  $12.5 \text{ km} \times 12.5 \text{ km}$  ASCAT scatterometer reference ground truth, for the whole CSK<sup>®</sup> SAR data set. **(a)** Wind speed scatter plot. **(b)** Wind direction scatter plot.

## 4.2 Sea wave numerical simulations

In this subsection, sea wave numerical simulations accomplished through the SWAN model are described with respect to some relevant wave storms recorded in the considered test area during the winter season of 2010 (see Table 2). In all the experiments,  $H_S$  and  $T_D$  are used as reference parameters at the output of the SWAN simulations. The latter are properly undertaken by using different wind field forcings, i.e., ECMWF model winds, SAR-based wind field estimations and ECMWF-SAR blended wind field products. For comparison purposes, buoy-derived data are used as reference ground truth information.

The first experiment is relevant to the wave storm of 8–10 November 2010, which exhibits the maximum time evolution ( $T_D = 55 \text{ h}$ ) with respect to the other storms, and is associated to a strong atmospheric perturbation (see Table 2). The  $H_S$  values, obtained by forcing the SWAN model with the above-mentioned wind field products, are plotted against the time evolution of the wave storm (see Fig. 5). A first visual analysis shows that the  $H_S$  profile obtained with ECMWF model winds (blue line) does not fit that of the reference buoys (red line), with a strong  $H_S$  overestimation (38 %) over the correctly retrieved time evolution of the storm ( $T_D = 55 \text{ h}$ ). Conversely, the  $H_S$  profiles obtained with SAR-derived wind field estimations (green line) and ECMWF-SAR blended wind field products (black line)

**Table 2.** Wave storms of winter season 2010 used for both SWAN simulation and CVA purposes.

Wave Storm	Reference Buoy				ECMWF		SAR		ECMWF-SAR	
	$H_S$ (m)	$T_P$ (s)	$D_W$ (° N)	$T_D$ (h)	$H_S$ (m)	$T_D$ (h)	$H_S$ (m)	$T_D$ (h)	$H_S$ (m)	$T_D$ (h)
8–10 Nov 2010	4.23	9.5	218	55	5.5	55	2.4	55	3.65	55
17–18 Dec 2010	5.01	9.5	231	24	5.0	24	2.5	15	3.4	15
23–25 Dec 2010	4.29	10	255	48	4.0	53	2.4	48	3.4	48

**Table 3.** Beach width classification of the different stretches along the Sele coastal plain.

$L$ (m) (2010)	Mouth of Picentino (P3–P4)		Mouth of Tuscano (P5–P6–P7)		Mouth of Sele (P1–P2)		Mouth of Solofrone (P8–P9–P10)	
	Extension (m)	(%)	Extension (m)	(%)	Extension (m)	(%)	Extension (m)	(%)
Wide ( $L > 50$ )	–	–	800	32	–	–	1200	60
Medium ( $20 < L < 50$ )	1200	48	1700	68	2050	82	800	40
Restricted ( $L < 20$ )	1300	52	–	–	350	14	–	–
Defense works	–	–	–	–	100	4	–	–

well fit that of the reference buoys, providing a correct retrieval of the storm evolution (see  $T_D$  values in Table 2). In detail, the ECMWF-SAR blended wind field product exhibits a smaller  $H_S$  underestimation (9%) with respect to the SAR one (40%). A deeper analysis (see Table 2) shows that the maximum  $H_S$  value obtained by using ECMWF model winds (blue line) and SAR-based wind field estimations (green line) is overestimated ( $H_S = 5.5$  m) and underestimated ( $H_S = 2.4$  m), respectively, with respect to the reference buoy data ( $H_S = 4.23$  m). Conversely, a much better accordance is experienced with the ECMWF-SAR blended wind field product ( $H_S = 3.5$  m, see the black line). This latter result takes into account that ECMWF model winds cover a wide spatial domain with dense temporal sampling, while SAR-derived wind field estimations are sample local measurements obtained over a wide spatial domain. Since the dense temporal sampling of wind field forcing is necessary to get reliable SWAN simulation results, it is mandatory to provide denser temporal SAR-based wind field estimations. As a matter of fact, the ECMWF-SAR blended wind field product is here provided as the most straightforward solution to overcome the problem in question. In detail, experimental results demonstrate the effectiveness of the ECMWF-SAR blended wind field product for a suitable description of the wave storm in terms of  $H_S$  and  $T_D$ , see Table 3.

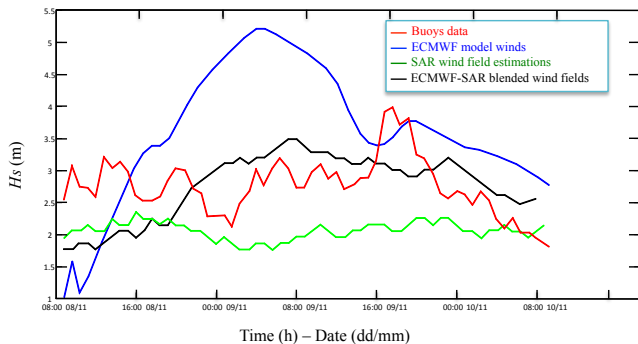
The second experiment is relevant to the wave storm of 17–18 December 2010, which exhibits the maximum wave height ( $H_S = 5.01$  m) and the minimum time evolution ( $T_D = 24$  h) among the other wave storms (see Table 2 and Fig. 6). The  $H_S$  values, obtained by forcing the SWAN model with the above-mentioned wind field products, are plotted against the time evolution of the wave storm (see Fig. 6). A first visual analysis shows that the  $H_S$  profiles obtained with the

three above-mentioned wind field forcings well fit the reference one (red line). A deeper analysis shows that ECMWF model winds (blue line) are in perfect agreement with the reference buoys' data (red line), in terms of both the maximum  $H_S$  value ( $H_S = 5$  m) and wave storm time evolution ( $T_D = 24$  h). Conversely, SAR-based wind field estimations (green line) and ECMWF-SAR wind field products (black line) exhibit a general  $H_S$  underestimation with respect to the reference buoys' data (blue line), although they are both able to correctly retrieve the time evolution of the storm (see  $T_D$  values in Table 2). In detail, the maximum  $H_S$  values obtained through SAR ( $H_S = 2.5$  m) and ECMWF-SAR blended wind field products ( $H_S = 3.4$  m) demonstrates a smaller  $H_S$  underestimation for the ECMWF-SAR blended product (32%) with respect to the SAR one (50%); see Table 3. This result is most likely due both to the faster time evolution of the wave storm with respect to the previous wave storm and to the underestimation of SAR-based wind field retrievals. However, experimental results demonstrate the effectiveness of the ECMWF-SAR blended wind field product for a suitable description of the wave storm in terms of  $H_S$  and  $T_D$  values, see Table 3.

The third experiment is relevant to the wave storm of 23–25 December 2010, which exhibits a maximum  $H_S$  value equal to 4.29 m and a time evolution  $T_D$  of 48 h (see Table 2). The  $H_S$  values, obtained by forcing the SWAN model with the above-mentioned wind field products, are plotted against the time evolution of the wave storm (see Fig. 7). Experimental results show that the  $H_S$  profiles obtained with the three above-mentioned wind field forcings well fit that of the reference buoys (red line) and are able to catch the maximum energetic peak of the storm, see Fig. 7. In detail, ECMWF model winds (blue line) provide a consistent  $H_S$  retrieval

**Table 4.** Morpho-sedimentary features and CVA parameters for each profile of Sele coastal plain.

	P1	P2	P3	P4	P5	P6	P7	P8	P9	P10
$\mu_s$ (mm)	5.037	0.971	0.753	0.687	4.487	0.444	0.493	0.341	0.396	0.346
$L$ (m)	20.4	27.3	20.4	26.2	26.3	25.5	15.8	41.6	57.7	47.1
$\beta$ (%)	11.2	10.1	9.6	13.7	5.7	14.7	11.9	6.8	5.9	15.0
$V_E$ (m yr <sup>-1</sup> )	0.71		1.20		2.17			0.08		
$E$	2 (Low)		3 (Moderate)		4 (High)			1 (Stable)		

**Fig. 5.** Simulated and measured significant wave height  $H_S$  for the winter storm of 8–10 November 2010. Comparison among buoys' data (red line), ECMWF (blue line), SAR (green line), and ECMWF-SAR blended wind fields (black line).

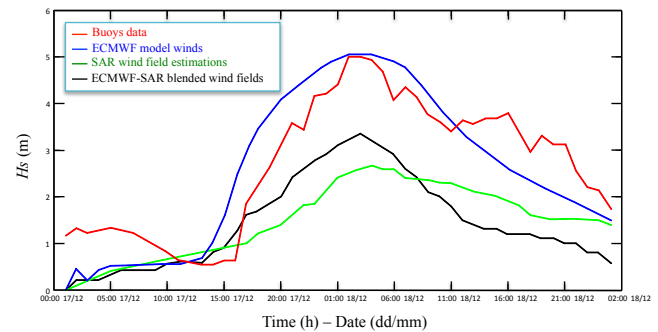
$H_S = 4$  m) with respect to that of the reference buoys, although they exhibit a slight  $T_D$  overestimation (9%). Conversely, SAR-derived wind field estimations (green line) and ECMWF-SAR blended wind field products (black line) exhibit a significant (44%) and slight (20%)  $H_S$  underestimation, respectively, although they are both able to retrieve the time evolution of the storm (see  $T_D$  values in Table 2). Again, experimental results demonstrate the effectiveness of the ECMWF-SAR blended wind field product for a suitable description of the wave storm in terms of  $H_S$  and  $T_D$  profiles.

In summary, all the experimental results demonstrate the benefits of the ECMWF-SAR blended wind field product, which can retrieve wind wave interaction parameters for the effective wave storm description, in terms of time evolution  $T_D$  and maximum  $H_S$  value.

### 4.3 CVA experiments

In this subsection, some meaningful CVA results are discussed with respect to the three relevant wave storms described in Table 2. The reference test area is the Sele coastal plain, which has shown a high sensitivity to major flood risk as reported in Alberigo et al. (2012).

Based on the SWAN simulating results described in the Sect. 4.2, the CVA is here accomplished by evaluating  $I_{Ru}$ ,  $I_R$ ,  $E$  and  $I_i$  through the SWAN-based interaction parameters

**Fig. 6.** Simulated and measured significant wave height  $H_S$  for the winter storm of 17–18 December 2010. Comparison among buoys' data (red line), ECMWF (blue line), SAR (green line) and ECMWF-SAR blended wind fields (black line).

that have been retrieved by using both ECMWF model winds and ECMWF-SAR blended wind fields. For comparison purposes, buoy-derived information is used, together with the coastal wave climate and the morpho-sedimentary features of the test area, to retrieve reference  $I_{Ru}$ ,  $I_R$ ,  $E$  and  $I_i$  profiles (Di Paola, 2011; Alberigo et al., 2012).

Firstly, a brief analysis of the Sele Coastal plain is provided with respect to some meaningful coastal morpho-sedimentary features. In Fig. 8, the elevation map of the test area is shown in gray tones together with the position of ten specific elevation transects (from P1 to P10), each of which encompasses the intertidal and emerged beach elevation as shown in Fig. 9. The longitudinal extensions of the beach are given in Table 3 together with both their relative percentage value and their longitudinal extensions. The low coastline under study presents different morphological and anthropic features, which allow distinguishing some different stretches of coastline (see Tables 3 and 4): (1) the first one, extending from the mouth of river Picentino till the river Asa (P1 and P2 transects), shows small beaches and strong urbanization, with gravely ( $\mu_s = 5.037$  mm) and sandy ( $\mu_s = 0.971$  mm) sediments for P1 and P2 transects, respectively (see Table 4). These profiles are classified as medium ( $20 < L < 50$ ) and restricted ( $L < 20$ ) emerged beach for about 48% (1200 m) and 52% (1300 m) of their total extension (2500 m), respectively (see Table 3); (2) the second one,

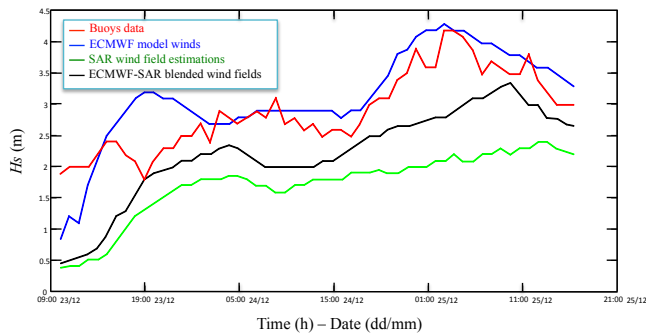


**Fig. 7.** Simulated and measured significant wave height  $H_S$  for the winter storm of 23–25 December 2010. Comparison among buoys' data (red line), ECMWF (blue line), SAR (green line) and ECMWF-SAR blended wind fields (black line).

around the mouth of the river Tusciano, is characterized by a well-preserved and stable dune system (P3 and P4 transects), with sandy ( $\mu_s = 0.753$  mm) and finer sandy ( $\mu_s = 5.037$  mm) sediments for P3 and P4 transects, respectively (see Table 4). These profiles are classified as wide ( $L > 50$ ) and medium ( $20 < L < 50$ ) emerged beaches for about 32 % (800 m) and 68 % (1700 m) of their total extension (2500 m), respectively (see Table 3); (3) the third one, i.e., the area between the mouths of rivers Tusciano and Sele (P5 and P6 transects), is characterized by eroded and deteriorated dunes, with gravelly ( $\mu_s = 4.487$  mm) and finer sandy ( $\mu_s = 0.444$  mm) sediments for P5 and P6 transects, respectively (see Table 4). On the left bank of river Sele, an intense anthropogenic load is also experienced (P7 transect), which is characterized by finer sandy ( $\mu_s = 0.444$  mm) sediments (see Table 4). These profiles are classified as medium ( $20 < L < 50$ ) and restricted ( $L < 20$ ) emerged beach for about 82 % (2050 m) and 14 % (350 m) of their total extension (2500 m), respectively, with the presence of defense works for the remaining 100 m (4 %) (see Table 3); (4) the fourth one, which extends from the cities of Paestum and Agropoli (P8, P9 and P10 transects), is characterized by wider beaches with both well-preserved dunes and low anthropic load. These profiles exhibit fine sandy sediments ( $\mu_s$  is equal to 0.341 mm, 0.396 mm and 0.346 mm for P8, P9 and P9 transects, respectively) and are classified as wide ( $L > 50$ ) and medium ( $20 < L < 50$ ) emerged beaches for about 60 % (1200 m) and 40 % (800 m) of their total extension (2500 m), respectively (see Tables 3 and 4).

Based on the description and the classification of the morpho-sedimentary features of the test area (see Tables 3 and 4),  $I_{Ru}$ ,  $I_R$ ,  $E$  and  $I_i$  profiles are evaluated over the ten transects in Figs. 8 and 9, according to the CVA approach described in Sect. 3.3. First of all, experimental results relevant to the reference buoys' data are discussed to provide the reference vulnerability information for the considered transects. Then a comparative analysis is presented with respect to the reference buoys' data to analyze the performances

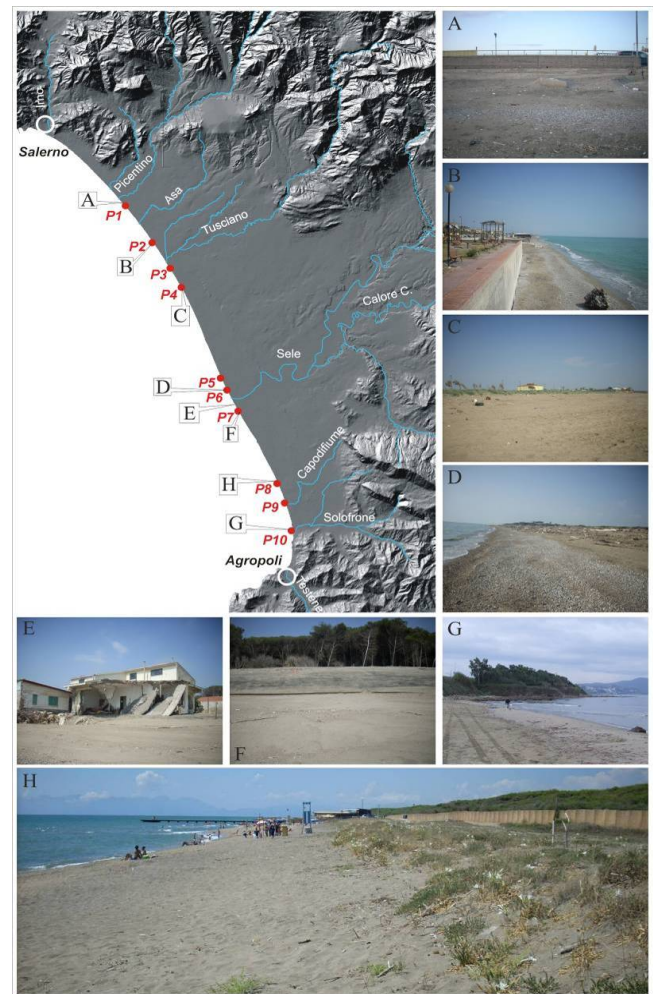


**Fig. 8.** Detail of the Sele coastal plain: (A) profile P1 without dune; (B) the littoral zone, near the P2 profile; (C) dune on profile P4 with the presence of pioneer vegetation; (D) emerged and tidal beach on P6 profile; (E) house belonging to the village Merola, located at the left bank of the Sele mouth; (F) Profile P7, with carved dune; (G) the end of physiographic unit near profile P10; (H) dune and emerged beach of profile P8 with the presence of pioneer vegetation on the dune. All the beach profiles are detailed in Fig. 9.

of both ECMWF model winds and ECMWF-SAR blended wind field products for CVA purposes.

In Fig. 10 the  $X_{max}/L$  % profile, obtained through the reference buoys' data (purple bars), the ECMWF model winds (red bars) and the ECMWF-SAR blended wind field product (yellow bars), is shown together with the associated  $I_{Ru}$  values for the three reference wave storms. As clearly shown by the reference buoys' data (purple bars), the lowest  $X_{max}/L$  % values are experienced for P8-P9-P10 transects that correspond to the areas with greater  $L$  values (see Table 4). This result highlights the stronger impact of  $L$  with respect to  $\beta_f$  (here approximated to  $\beta$ ) for the evaluation of  $X_{max}/L$  % and  $X_{max}$ , respectively. In fact, on the one hand,  $X_{max}/L$

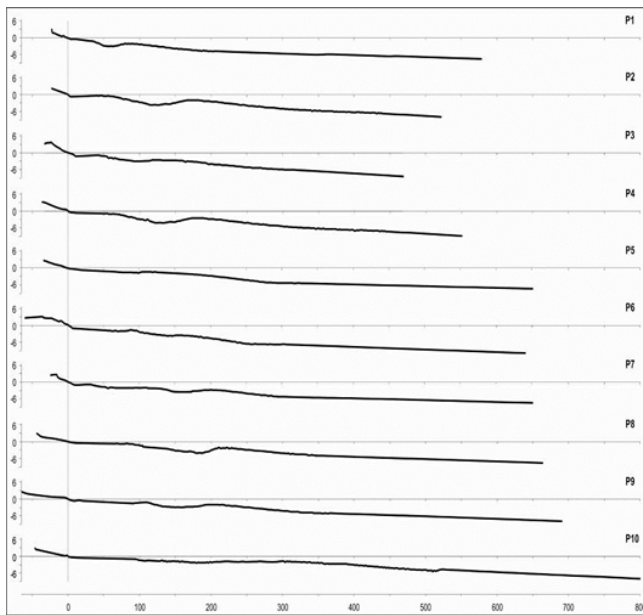


**Fig. 9.** Topographical beach profiles carried out in the Sele coastal plain.

% is inversely proportional to  $L$ , therefore it is minimum for the maximum  $L$  values, which correspond to P8, P9 and P10 transects (see Table 4). On the other hand,  $X_{\max}$  is inversely proportional to  $\beta$ , therefore it is minimum for the maximum  $\beta$  values, which correspond to P4, P6 and P10 transects (see Table 4). In addition to this, it can be noted that  $X_{\max}/L$  % is greater from P1 to P7 transects with the maximum value reached at P7 beach profile, which exhibits the lowest  $L$  value and then represents the most critical case in terms of short-term vulnerability risk (see Table 4). Experimental results show that the  $X_{\max}/L$  % profile is the same for the three reference wave storms (see Fig. 10). In detail, the most pronounced results are experienced for the second storm (see Fig. 10b), which exhibits the greatest  $H_S$  value among the three wave storms. This result shows the key role played by  $H_S$  for the evaluation of  $X_{\max}$ , which reaches the maximum for the greatest retrieved  $H_S$  value.

Based on the classification rule defined for  $I_{Ru}$  (see Sect. 3.3) and according to the  $X_{\max}/L$  % values obtained for the three reference wave storms, it is possible to define the short-term vulnerability risk associated to  $I_{Ru}$  for each transect of the considered test area. In detail, with respect to the first and the third wave storms, a stable ( $I_{Ru} = 1$ ), low ( $I_{Ru} = 2$ ), medium ( $I_{Ru} = 3$ ) and high ( $I_{Ru} = 4$ ) short-term vulnerability risk is experienced for P10, P8-P9, P2-P4-P6 and P1-P3-P5-P7 transects, respectively. With respect to the second wave storm, a low ( $I_{Ru} = 2$ ), medium ( $I_{Ru} = 3$ ) and high ( $I_{Ru} = 4$ ) short-term erosion value is experienced for P9-P10, P8, and P1-P2-P3-P4-P5-P6-P7 transects, respectively. All the results demonstrate that P7 is the most critical case among the ten considered transects, since it exhibits the

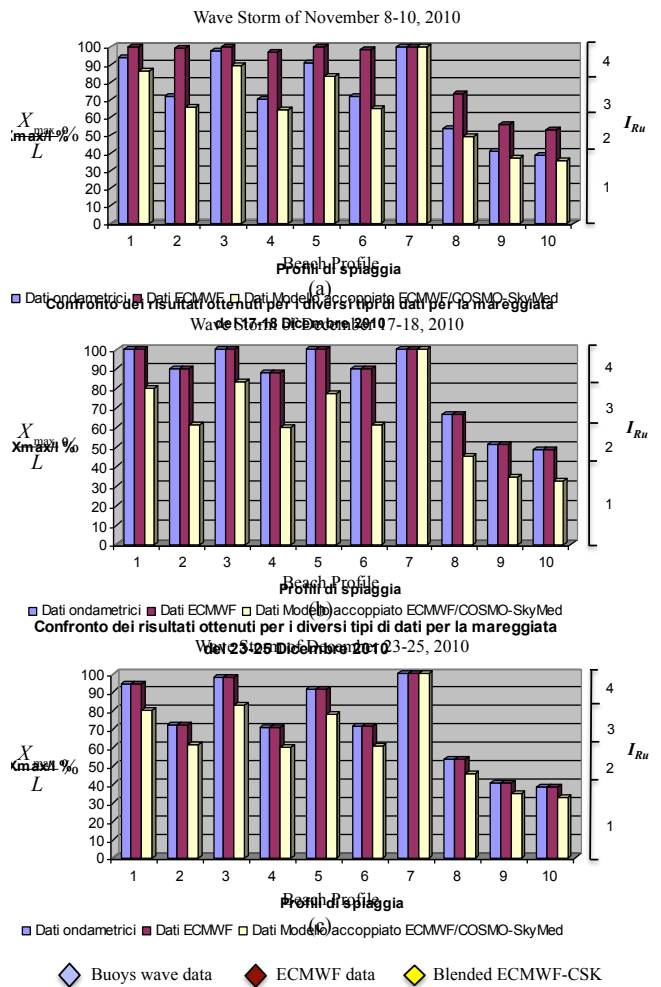


**Fig. 10.**  $X_{\max}/L$  % and  $I_{Ru}$  values, obtained through the buoys' data (purple bars), ECMWF model winds (red bars) and ECMWF-SAR blended wind field products (yellow bars), for the ten beach profiles of the considered test area. (a) Wave storm of 8–10 November 2010. (b) Wave storm of 17–18 December 2010. (c) Wave storm of 23–25 December 2010.

highest  $X_{\max}/L$  % value and then is the most exposed profile in terms of short-term vulnerability risk.

Following this preliminary analysis, the comparison between the reference buoys' data (purple bars) and both ECMWF (red bars) and ECMWF-SAR blended wind field products (yellow bars) is properly discussed; see Fig. 10. On the one hand, it can be noted that the  $X_{\max}/L$  % profile and the corresponding  $I_{Ru}$  values, obtained through ECMWF model winds for the ten considered transects, are in perfect agreement with the reference buoys' data (purple bars) for the second and the third wave storms. Conversely, a non-negligible overestimation (30 %) of both  $X_{\max}/L$  % profile and therefore  $I_{Ru}$  values is experienced with respect to the first wave storm. These results take into account that ECMWF model winds correctly retrieve the maximum  $H_S$

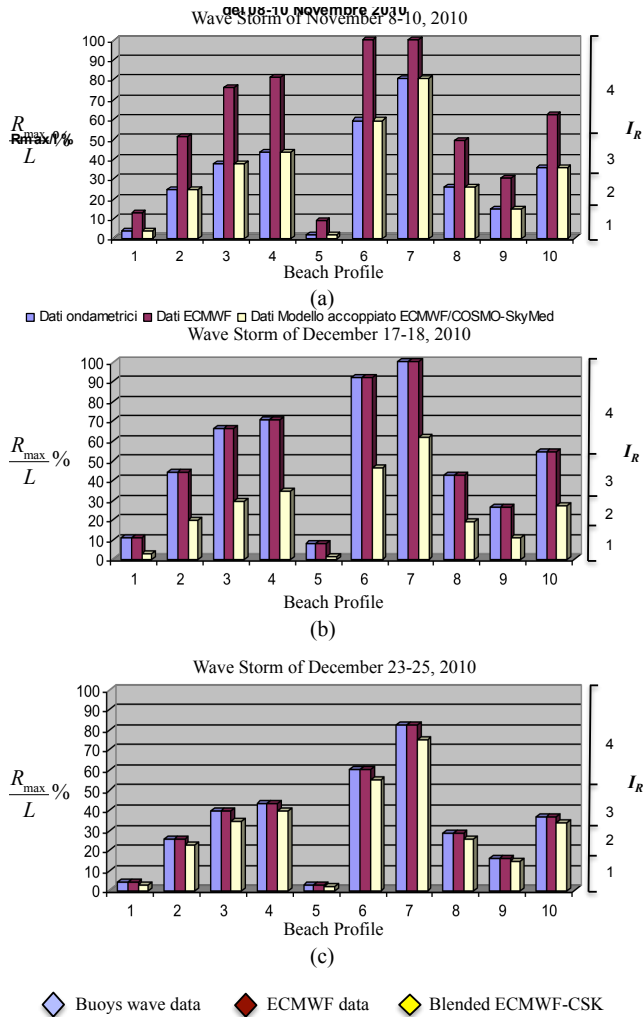


**Fig. 11.**  $R_{\max}/L$  % profile and  $I_R$  values, obtained through the buoys' data (purple bars), ECMWF model winds (red bars) and ECMWF-SAR blended wind field products (yellow bars), for the ten beach profiles of the considered test area. (a) Wave storm of 8–10 November 2010. (b) Wave storm of 17–18 December 2010. (c) Wave storm of 23–25 December 2010.

value for the second and the third wave storms, with a pronounced  $H_S$  overestimation for the first wave storm (see Sect. 4.2). On the other hand, it can be noted that the  $X_{\max}/L$  % profile and the corresponding  $I_{Ru}$  values, obtained through ECMWF-SAR blended wind field products for the ten considered transects (yellow bars), well fit the reference buoys' data for the first and the third wave storms, with a non-negligible disagreement for the second wave storm. In detail, a pronounced  $X_{\max}/L$  % underestimation (30 %) is provided for the second wave storm, which severely impacts the  $I_{Ru}$  evaluation, thus providing underestimated short-term vulnerability risk values. Conversely, a slight  $X_{\max}/L$  % underestimation (15 %) is provided for the third wave storm, which does not impact the evaluation of  $I_{Ru}$  index. These results take

into account that ECMWF-SAR blended wind field products correctly retrieve the maximum  $H_S$  value for the first wave storm, with an  $H_S$  underestimation for the second and the third wave storms (see Sect. 4.2).

In Fig. 11 the  $R_{\max}/L$  % profile, obtained through reference buoys' data (purple bars), ECMWF model winds (red bars) and ECMWF-SAR blended wind field products (yellow bars), is shown together with the associated  $I_R$  values for the three reference wave storms. As clearly shown by the reference buoys' data (purple bars), the lowest values of  $R_{\max}/L$  % are experienced for P1 and P5 transects that correspond to the areas where the beach sediments show the greater  $\mu_s$  values (see Table 4). This result can be explained by considering that  $R_{\max}$  is inversely proportional to  $\mu_s$ , which plays a key role for the evaluation of both  $T_s$  and  $W_b$  within Eq. (7). Moreover, it can be noted that  $R_{\max}/L$  % profile is the same for all the three reference wave storms. The most pronounced results are obtained for the second wave storm, which exhibits both the greatest  $H_S$  and the lowest  $T_D$  values (see Table 2). This result takes into account that  $R_{\max}$  is directly proportional to  $H_S$  and inversely proportional to  $T_D$ ; see Eqs. (7) and (8). In fact, on the one hand, high  $H_S$  values provide high  $S$ ,  $d_b$  and then  $R_{\max}$  values. On the other hand, low  $T_D$  value provides the reduction of  $\gamma$ , which in turn provides high  $R_{\max}$  values. This means that for a given  $H_S$  value, wave storms with lower  $T_D$  value exhibit higher  $R_{\max}/L$  % profiles. In addition to this it is shown that, for the three reference wave storms, the maximum  $R_{\max}/L$  % value is experienced at P7 transect, which exhibits the lowest  $L$  value among the ten beach profiles and then is the most critical case in terms of short-term vulnerability risk (see Table 4). This result highlights the impact of  $L$  for the evaluation of  $R_{\max}/L$  %.

Based on the classification rule defined for  $I_R$  (see Sect. 3.3) and according to the  $R_{\max}/L$  % values experienced for the three reference wave storms, it is possible to define the short-term vulnerability risk associated to  $I_R$  for each transect of the considered test area. With respect to the first and the third wave storms, a stable ( $I_R = 1$ ), low ( $I_R = 2$ ), medium ( $I_R = 3$ ) and high ( $I_R = 4$ ) short-term vulnerability risk is experienced for P1–P5–P9, P2–P8, P3–P4–P10 and P6–P7 transects, respectively. With respect to the second wave storm, a stable ( $I_R = 1$ ), low ( $I_R = 2$ ), medium ( $I_R = 3$ ) and high ( $I_R = 4$ ) short-term vulnerability risk is experienced for P1–P5, P9, P2–P8 and P3–P4–P6–P7–P10 transects, respectively. All the results clearly show that P7 is the most critical case among the ten considered transects, since it exhibits the highest  $R_{\max}/L$  % value and then is the most exposed beach profile in terms of short-term vulnerability risk.

Following this preliminary analysis, the comparison between the reference buoys' data (purple bars) and both ECMWF (red bars) and ECMWF-SAR blended wind field products (yellow bars) is properly discussed; see Fig. 11. Experimental results agree with the ones obtained for  $X_{\max}/L$  %. On the one hand, ECMWF model winds exhibit a good agreement with the reference buoys' data for the second

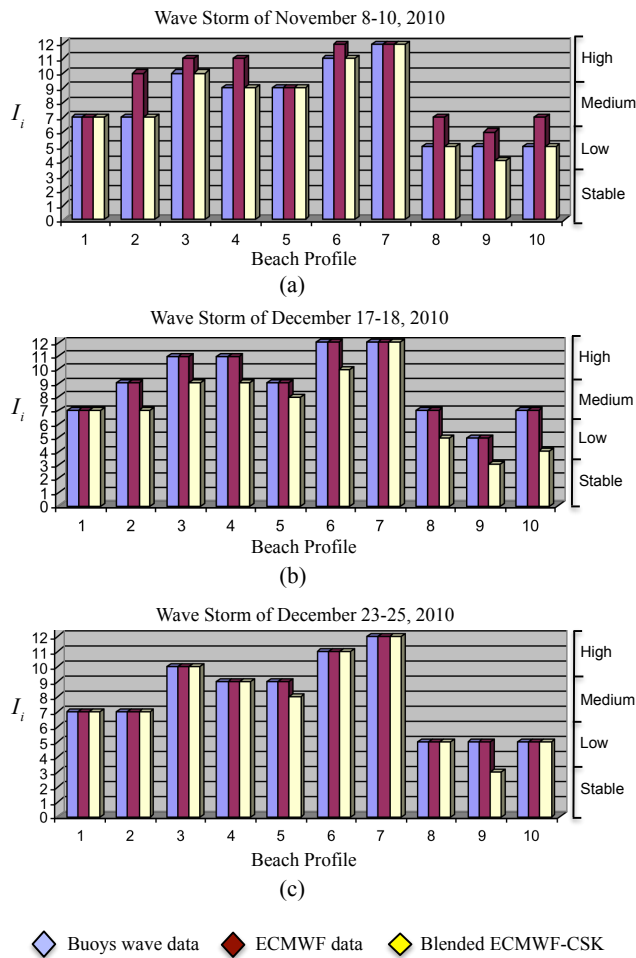


**Fig. 12.**  $I_i$  values and vulnerability risk classification, obtained through buoys' data (purple bars), ECMWF model winds (red bars) and ECMWF-SAR blended wind fields (yellow bars), for the ten beach profiles of the considered test area. (a) Wave storm of 8–10 November 2010. (b) Wave storm of 17–18 December 2010. (c) Wave storm of 23–25 December 2010.

and the third wave storms, while a pronounced overestimation (100 %) is provided for the first wave storm. This result takes into account the  $H_S$  overestimation provided by ECMWF model winds for the first wave storm (about 30 %), which in turn provides overestimated  $R_{\max}/L$  % and short-term vulnerability risk values. On the other hand, ECMWF-SAR blended wind field products exhibit a good agreement with the reference buoys' data for the first wave storm, while they underestimate both  $R_{\max}/L$  % and  $I_R$  values for the second (50 %) and the third (10 %) wave storms. This result takes into account the  $H_S$  underestimation provided by ECMWF-SAR blended wind field products for the second and the third first wave storms, which in turn provides underestimated  $R_{\max}/L$  % and short-term vulnerability risk values.

In Table 4, the  $V_E$  profile, obtained through the long-term photogrammetric analysis, is shown together with  $E$  values

for each transect of the considered test area. Experimental results show that a stable ( $E = 1$ ), low ( $E = 2$ ), medium ( $E = 3$ ) and high ( $E = 4$ ) long-term vulnerability risk is experienced for P8-P9-P10, P1-P2, P3-P4 and P5-P6-P7 transects, respectively.

In Fig. 12, the impact index  $I_i$  and the coastal vulnerability risk classification, obtained through reference buoys' data (purple bars), ECMWF model winds (red bars) and ECMWF-SAR blended wind field products (yellow bars), is shown for the three reference wave storms. As clearly shown by the reference buoys' data (purple bars), the first and the third wave storms exhibit a low ( $4 \leq I_i \leq 6$ ), moderate ( $7 \leq I_i \leq 9$ ) and high ( $10 \leq I_i \leq 12$ ) vulnerability risk for P8-P9-P10, P1-P2-P4-P5 and P3-P6-P7 transects, respectively. With respect to the second wave storm, a low ( $4 \leq I_i \leq 6$ ), moderate ( $7 \leq I_i \leq 9$ ) and high ( $10 \leq I_i \leq 12$ ) vulnerability risk is experienced for P9, P1-P8-P10, P2-P3-P4-P5-P6-P7-P9 transects, respectively. Experimental results clearly show that P7 is the most critical case among the ten considered transects, since it exhibits the highest  $I_i$  value and thus is the most exposed beach profile in terms of coastal vulnerability risk.

Following this preliminary analysis, the comparison between the reference buoys' data (purple bars) and both ECMWF (red bars) and ECMWF-SAR blended wind field products (yellow bars) is properly discussed; see Fig. 12. On the one hand, ECMWF model winds exhibit a good agreement with the reference buoys' data for the second and the third wave storms, while a slight overestimation (15 %) is observed for the first wave storm. On the other hand, ECMWF-SAR blended wind field products exhibit a good agreement with the reference buoys' data for the first and the third wave storm, while they underestimate  $I_i$  values for the second (15 %) wave storm. These results take into account both the SWAN simulating results described in Sect. 4.2 and the short-term coastal vulnerability analysis provided in terms of  $I_{Ru}$  and  $I_R$  profiles. Experimental results clearly show that the  $I_i$  overestimation (underestimation) provided by ECMWF (ECMWF-SAR blended) wind field products is always lower than the one experienced for  $I_{Ru}$  and  $I_R$  profiles. This result takes into account that  $I_i$  is evaluated over a certain range of values associated to both short- ( $I_{Ru}$  and  $I_R$ ) and long-term ( $E$ ) erosion indexes. Therefore, it allows consistent reduction of the differences experienced for each single considered index, especially for  $I_{Ru}$  and  $I_R$ .

In summary, experimental results demonstrate the benefits of the ECMWF-SAR blended wind field product, which allows consistent retrieval of short-term ( $I_{Ru}$  and  $I_R$ ) and long-term ( $I_i$ ) vulnerability risk parameters for the effective CVA analysis of the considered test area.

## 5 Conclusions

In this paper the capabilities of CSK<sup>®</sup> SAR data are first investigated to provide surface wind fields for the improvement

of wind wave modeling and coastal vulnerability assessment purposes. The SAR data set consists of 60 X-band VV-polarized Level 1B DGM ScanSAR Huge Region CSK<sup>®</sup> SAR measurements, collected in the test area of the southern Tyrrhenian Sea basin during the winter season of 2010. The SAR-based wind speed estimation is provided by means of the azimuth cut-off procedure, while the SAR-based wind direction retrieval is achieved by using the MRA-DWT approach. The wind wave modeling is based on the third-generation SWAN model, while the CVA is provided by means of a key parameter known as impact index ( $I_i$ ). Experimental results have shown the following:

- X-band CSK<sup>®</sup> SAR data can be effectively used as alternative resource for sea surface wind field retrieval purposes. The consistency of X-band CSK<sup>®</sup> SAR-derived wind field retrievals is validated with respect to the ASCAT scatterometer ground truth. Experimental results demonstrate the effectiveness of the azimuth cut-off procedure and the MRA-DWT technique to retrieve the wind speed and wind direction at sea with RMSE values of about  $2 \text{ m s}^{-1}$  and  $20^\circ$ , respectively.
- SWAN numerical simulations are run with respect to three reference winter wave storms of 2010, where three different wind field forcing (i.e. ECMWF, SAR and ECMWF-SAR blended winds) are effectively used to describe the wave storm events in terms of  $H_S$  and  $T_D$  profiles. The consistency of wind field forcings is validated with respect to national and regional buoy-derived information. Experimental results demonstrate the benefits of the ECMWF-SAR blended wind field product, which can retrieve SWAN-based wind wave interaction parameters, with a slight  $H_S$  underestimation at the storm peak (9–30 %).
- CVA is accomplished with respect to the three above-mentioned wave storms along ten beach profiles of the Sele coastal plain. Some meaningful vulnerability indexes (i.e.,  $I_{Ru}$ ,  $I_R$ ,  $E$  and  $I_i$ ) are evaluated through the SWAN-based wind wave interaction parameters that have been retrieved by using both ECMWF model winds and ECMWF-SAR blended wind field products. The consistency of these two wind field products is validated with respect to buoy-derived information. Experimental results demonstrate the benefits of the ECMWF-SAR blended wind field product, which allows retrieval of short-term ( $I_{Ru}$  and  $I_R$ ) and long-term ( $I_i$ ) vulnerability risk parameters for the effective CVA of the considered test area. Although ECMWF-SAR blended wind field products generally underestimate  $I_{Ru}$  (15–30 %) and  $I_R$  (10–50 %) profiles, they provide a slight  $I_i$  underestimation (15 %) that does not affect the vulnerability risk classification of the interested coastal area.

- Despite the limitations of dense temporal CSK<sup>®</sup> SAR acquisitions (and then SAR-derived wind field products), experimental results show that CSK<sup>®</sup> SAR-based wind field retrievals represents a valuable tool to improve coastal wind wave modeling, for both sea wave and CVA purposes.

*Acknowledgements.* COSMO-SkyMed<sup>®</sup> SAR data used in this study are provided by Italian Space Agency under the scientific research project entitled “Improvement of Oceanic Modeling for Coastal Management by means of COSMO-SkyMed<sup>®</sup> SAR data” (Project ID 1500). Authors would like to acknowledge Di Paola for beach morphological data and useful discussions.

Edited by: D. F. Prieto

## References

- Alberico, I., Amato, V., Aucelli, P. P. C., Di Paola, G., Pappone, G., and Roskopf, C. M.: Historical and recent changes of the Sele River coastal plain (Southern Italy): natural variations and human pressures, *Rendiconti Lincei*, 23, 3–12, doi:10.1007/s12210-011-0156-y, 2012.
- Benassai, G.: Introduction to coastal dynamics and shoreline protection, Wit Press, Southampton, 1, 1–356, 2006.
- Benassai, G. and Ascione, I.: Implementation and validation of wave watch III model offshore the coastlines of Southern Italy, in: Proceedings of 25th International Conference on Offshore Mechanics and Arctic Engineering 2006 – 92555, Hamburg, Germany, 4–9 June 2006, 553–560, 2006.
- Benassai, G., Chirico, F., and Corsini, S.: Una metodologia per la definizione del rischio da inondazione costiera, *Studi Costieri*, 16, 51–72, 2009.
- Booij, N., Ris, R. C., and Holthuijsen, L. H.: A third-generation wave model for coastal regions, Part I: Model description and validation, *J. Geophys. Res.*, 104, 7649–7666, 1999.
- Bruun, P.: Sea level rise as a cause of shore erosion, *J. WATERW PORT C-ASCE*, 88, 117–130, 1962.
- Carter, T. R., Parry, M. L., Nishioka, S., and Harasawa, H.: Technical guidelines for assessing climate change impacts and adaptation, University College London, London. Centre Glob. Environ. Res., Tskuba, Japan, 1994.
- Chapron, B., Fouhaily, T. E., and Kerbaol, V.: Calibration and validation of ERS wave mode products, *Inst. Fr. De Rech. pour l'Exploit. de la Mer*, Brest, France, Doc. DRO/OS/95-02, 1995.
- Diez, P. G., Perillo, G. M. E., and Picolo, M. C.: Vulnerability to sea-level rise on the coast of the Buenos Aires Province, *J. Coastal Res.*, 23, 119–126, 2007.
- Di Paola, G.: Geological and geo-morphological characterization of coastal Sele Plain (Campania, Italy) and considerations about its vulnerability, PhD Thesis, Università degli Studi del Molise, Italy, 2011.
- Du, Y., Vachon, P. W., and Wolfe, J.: Wind Direction Estimation from SAR images of the Ocean using Wavelet Analysis, *Can. J. Remote Sens.*, 28, 498–509, 2002.
- Gornitz, M. V., Daniels, R. C., White, T. W., and Birdwell, K. R.: The development of a coastal risk assessment database: vulner-

- ability to sea-level rise in the US southeast, *J. Coastal Res.*, 12, 327–338, 1994.
- Gornitz, V. M., Beaty, T. W., and Daniels, R. C.: A coastal hazards data base for the US West Coast, Carbon Dioxide Information Analysis Center, Oak Ridge National Laboratory, Oak ridge, Tennessee, 162 pp., 1997.
- Harlan Jr., J. A.: Short Time Scale Effects on High Frequency Radar-Derived Current Velocity Measurements, University of Colorado at Boulder, Ph.D. Dissertation, 2005.
- Hasselmann, K., Barnett, T. P., Bouws, E., Carlson, H., Cartwright, D. E., Enke, K., Ewing, J. A., Gienapp, H., Hasselmann, D. E., Kruseman, P., Meerburg, A., Müller, P., Olbers, D. J., Richter, K., Sell, W., and Walden, H.: Measurements of wind-wave growth and swell decay during the Joint North Sea Wave Project (JONSWAP), *Dtsch. Hydrogr. Z. Suppl.*, 12, 1–95, 1973.
- Holthuijsen, L. H., Booij, N., and Ris, R. C.: A spectral wave model for the coastal zone, in: Proceedings of the 2nd International Symposium on Ocean Wave Measurement and Analysis, New Orleans, 630–641, 1993.
- Holthuijsen, L., Booij, N., and Bertotti, L.: The propagation of wind errors through ocean wave hindcasts, *J. Offshore Mech. Arct. Eng.* 118, 184–189, 1996.
- Horstmann, J., Koch, W., and Lehner, S.: Wind Fields Retrieved from SAR in Comparison to Numerical Models, in Proceedings of Sixth International Winds Workshop, Madison, Wisconsin, USA, 7–10 May 2002, EUM. P., 35 pp., 2002.
- Italian Space Agency (ASI) – COSMO-SkyMed Mission: COSMO-SkyMed System Description and User Guide, Online, available at: <http://www.asi.it/it/flash/osservare/cosmoskymed/>, 2012.
- Janssen, P.: The Interaction of Ocean Waves and Wind, Cambridge University Press, UK, 2004.
- Johannessen, O. M., Sandven, S., Jenkins, A. D., Durand, D., Pettersson, L. H., Espedal, H., Evensen, G., and Hamre, T.: Satellite earth observation in operational oceanography, *Coast. Eng.*, 41, 155–176, 2000.
- Kerbaol, V., Chapron, B., and Vachon, P. W.: Analysis of ERS-1/2 Synthetic Aperture Radar wave mode images, *J. Geophys. Res.*, 103, 7833–7846, 1998.
- Korsbakken, E., Johannessen, J. A., and Johannessen, O. M.: Coastal Wind Field Retrievals from ERS Synthetic Aperture Radar Image, *J. Geophys. Res.*, 103, 7857–7874, 1998.
- Kriebel, D. L. and Dean, R. G.: Convolution method for time-dependent beach-profile response, *J. WATERW PORT C-ASCE*, 119, 204–207, 1993.
- Lee, P. H. Y., Barter, J. D., Beach, K. L., Hindman, C. L., Lake, B. M., Rungaldier, H., Shelton, J. C., Williams, A. B., Yee, R., and Yuen, H. C.: X band microwave backscattering from ocean waves, *J. Geophys. Res.*, 100, 2591–2611, 1995.
- Mallat, S. G.: A Theory for Multiresolution Signal Decomposition: the Wavelet Representation, *IEEE T. Pattern Anal.*, 11, 674–693, 1989.
- Migliaccio, M., Montuori, A., and Nunziata, F.: X-band Azimuth cut-off for wind speed retrieval by means of COSMO-SkyMed SAR data, in: Proceedings of IEEE/OES Baltic International Symposium, Klaipėda, Lithuania, 8–10 May 2012, 1–4, 2012.
- Monaldo, F. M., Thompson, D. R., Winstead, N. S., Pichel, W. G., Clemente-Colon, P., and Christiansen, M. B.: Ocean wind field mapping from synthetic aperture radar and its application to research and applied problems, *Johns Hopkins Apl. Tech. Dig.*, 26, 102–113, 2005.
- Montuori, A., Migliaccio, M., and Nunziata, F.: Wind Speed Estimation in the Tyrrhenian Sea by Means of X-band COSMO-SkyMed SAR Data, in: Proceedings of Tyrrhenian Workshop on Advances in Radar and Remote Sensing 2012, Naples, Italy, 12–14 September, 2012.
- Nicholls, R. J. and de la Vega-Leinert: Synthesis and up-scaling of sea-level rise vulnerability assessment studies (SURVAS): SURVAS methodology, Flood Hazard Research Centre – Middlesex University, 2000.
- Schiavulli, D., Sorrentino, A., and Migliaccio, M.: An Automatic Procedure for Scallop suppression and Homogeneity Analysis of Sea X-Band CSK<sup>®</sup> SAR Images, *Atti della Fondazione Giorgio Ronchi – Anno LXVII*, 66, 27–38, 2011.
- Schiavulli, D., Sorrentino, A., and Migliaccio, M.: An Innovative Technique for Postprocessing Descaloping, *IEEE Geosci. Remote S.*, 10, 424–427, 2012.
- Schulz-Stellenfleth, J. and Lehner, S.: Measurement of 2-D sea surface elevation fields using complex synthetic aperture radar data, *IEEE T. Geosci. Remote*, 42, 1149–1160, 2004.
- Stockdon, H. F., Holman, R. A., Howd, P. A., and Sallenger, A. H.: Empirical parameterization of setup, swash, and run-up, *Coast. Eng.*, 53, 573–588, 2006.
- Portabella, M.: Wind Field Retrieval from Satellite Radar Systems, Ph.D. Thesis, University of Barcelona, ISBN: 90-6464-499-3, 2002.
- Teixeira, J., Abreu, M., and Soares, C.: Uncertainty of ocean wave hindcasts due to wind modelling, *J. Offshore Mech. Arct. Eng.*, 117, 294–297, 1995.
- Tolman, H. L.: A third-generation model for wind waves on slowly varying, unsteady and inhomogeneous depths and currents, *J. Phys. Oceanogr.*, 21, 782–797, 1991.
- Tolman, H. L.: User manual and system documentation of WAVEWATCH-III version 1.15, Technical Note 151, NOAA/NWS/NCEP/OMB, Washington DC, United States, 97 pp., 1997.
- Tolman, H. L.: User manual and system documentation of WAVEWATCH-III version 1.18, Technical Note 166, NOAA/NWS/NCEP/OMB, Washington DC, US, 110 pp., 1999.
- Tolman, H. L.: User manual and system documentation of WAVEWATCH III version 3.14, Technical Note 276, NOAA/NWS/NCEP/MMAB, Washington DC, US, 194 pp., 2009.
- Yang, X., Li, X., Pichel, W. G., and Li, Z.: Comparison of Ocean Surface Winds From ENVISAT ASAR, MetOp ASCAT Scatterometer, Buoy Measurements, and NOGAPS Model, *IEEE Geosci. Remote*, 49, 4743–4750, 2011.
- WAMDI Group: The WAM model – A third generation ocean wave prediction model, *J. Phys. Oceanogr.*, 18, 1775–1810, 1988.
- Whitham, G. B.: Linear and Nonlinear Waves, John Wiley, New York, 636 pp., 1974.